Electronic Supplementary Information

Multifunctional Nanostructure of Au-Bi_2O_3 Fractals for CO_2 Reduction and Optical Sensing

Thanh Tran-Phu[†a], Rahman Daiyan[†b], Zelio Fusco[†a], Zhipeng Ma,[b] Lina Raihana Abd Rahim[a], Alexander Kiy[d], Patrick Kluth[d], Xuyun Guo[d], Ye Zhu[d], Hongjun Chen[a], Rose Amal[b], Antonio Tricoli[a]

[a] Nanotechnology Research Laboratory, College of Engineering and Computer Science, The Australian National University, Canberra, ACT 2601, Australia

[b] Particles and Catalysis Research Laboratory, School of Chemical Engineering, The University of New South Wales, Sydney, NSW 2052, Australia

[c] Department of Electronic Materials Engineering, Research School of Physics, Australian National University, Canberra, ACT 2601, Australia

[d] Department of Applied Physics, the Hong Kong Polytechnic University, Hung Hom, Hong Kong, PR China.

[†] Authors contributed equally,

Corresponding Authors
*Email: antonio.tricoli@anu.edu.au
r.amal@unsw.edu.au

Fractal Analysis

In this analysis, we used FracLac (an open-source plugin run in ImageJ)[1-3], which uses a "box counting" method to find the fractal dimension (D_f) and lacunarity (Λ) on the pixel distribution of a SEM images of samples. Typically, D_f of an object shows the similar patterns evolving through different length-scales and follows the power law.[4-5]

$$N = k_0 \left(\frac{r_g}{r} \right)^{D_f} \tag{S1}$$

where N is the number of monomers, k_o is a constant prefactor of order unity, r_g is the overall aggregate radius or gyration radius, r is radius of monomer. By defining $\varepsilon = r/r_g$, equation S1 can be written as:

$$N = k_0 \left(\varepsilon\right)^{-D_f} \tag{S2}$$

Equation S2 can be reshaped after taking logarithm of both sizes as follows:

$$\ln(N) = \ln(k_0) - D_f \ln\left(\varepsilon\right) \tag{S3}$$

Then fractal dimension can be evaluated from the slope (D_f) of equation S3 where the x-axis is $\ln(\varepsilon)$ and the y-axis is $\ln(N)$.

After obtaining SEM images, the foreground pixels with box size ε were counted during the scan, and 12 different box sizes were set. The generated fractal after scans were used to evaluate the D_f by taking an average of $\ln(N)$ and $\ln(\varepsilon)$.

For each box size ε the mean, μ, and the standard deviation, σ, for each box size were calculated. Then the lacunarity, Λ, was evaluated for each box size as $\Lambda = (\sigma / \mu)^2$, and the average lacunarity was computed as $\Lambda = \frac{1}{n} \sum_i (\sigma / \mu)^2 + 1$.

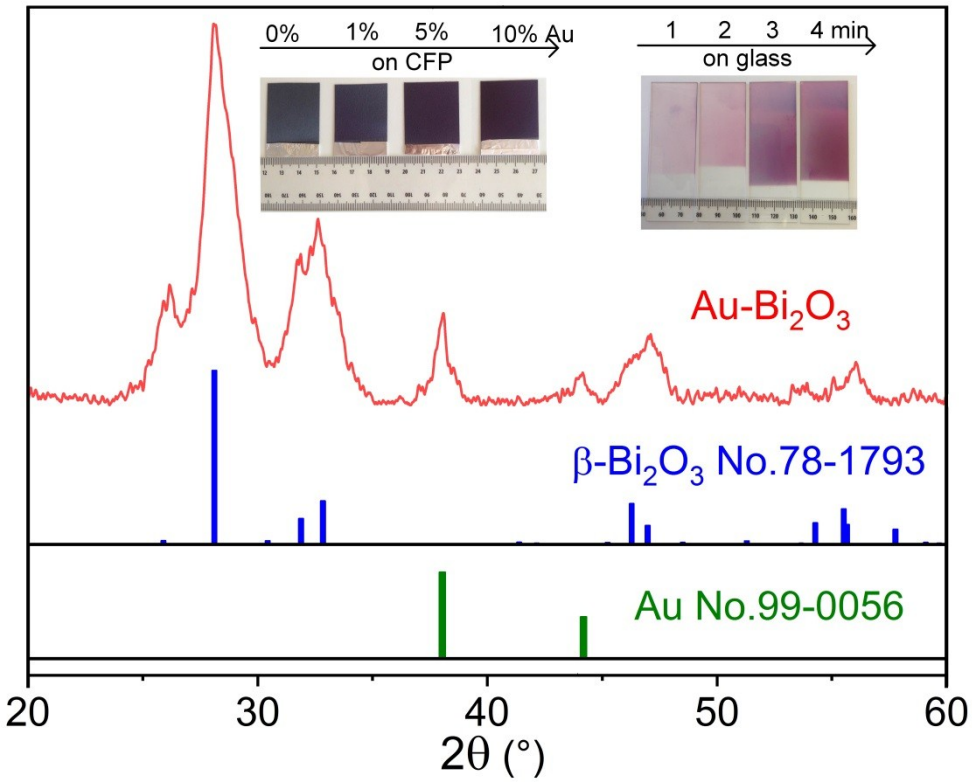

Figure S1. XRD of the Au-Bi_2O_3 fractal with references of Au and Bi_2O_3 patterns: inset are optical images of Au-Bi_2O_3 fabricated on CFP at different Au concentrations and on glass at different deposition times.

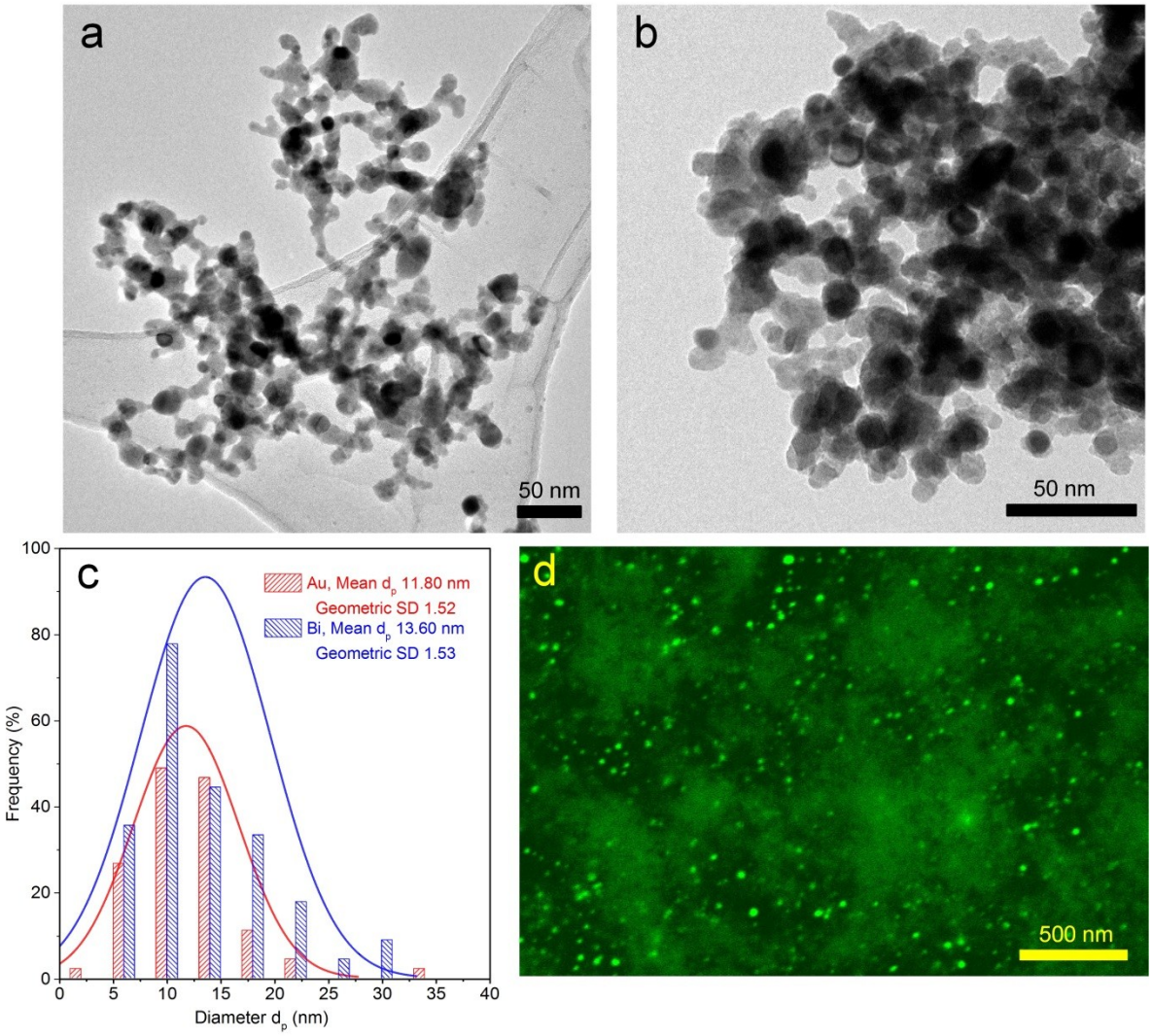

Figure S2. (a,b) TEM images of the Au-Bi_2O_3 with 5% of Au at different magnifications, (c) histogram of the particle distribution of the Au and Bi_2O_3, showing that Au and Bi_2O_3 have average particle sizes of 11.8 nm and 13.6 nm respectively, and (d) the top-view SEM image obtained with an angle-sensitive backscatter detector to provide difference in contrast of different atomic number elements: herein the Au nanoparticles are brighter than Bi_2O_3.

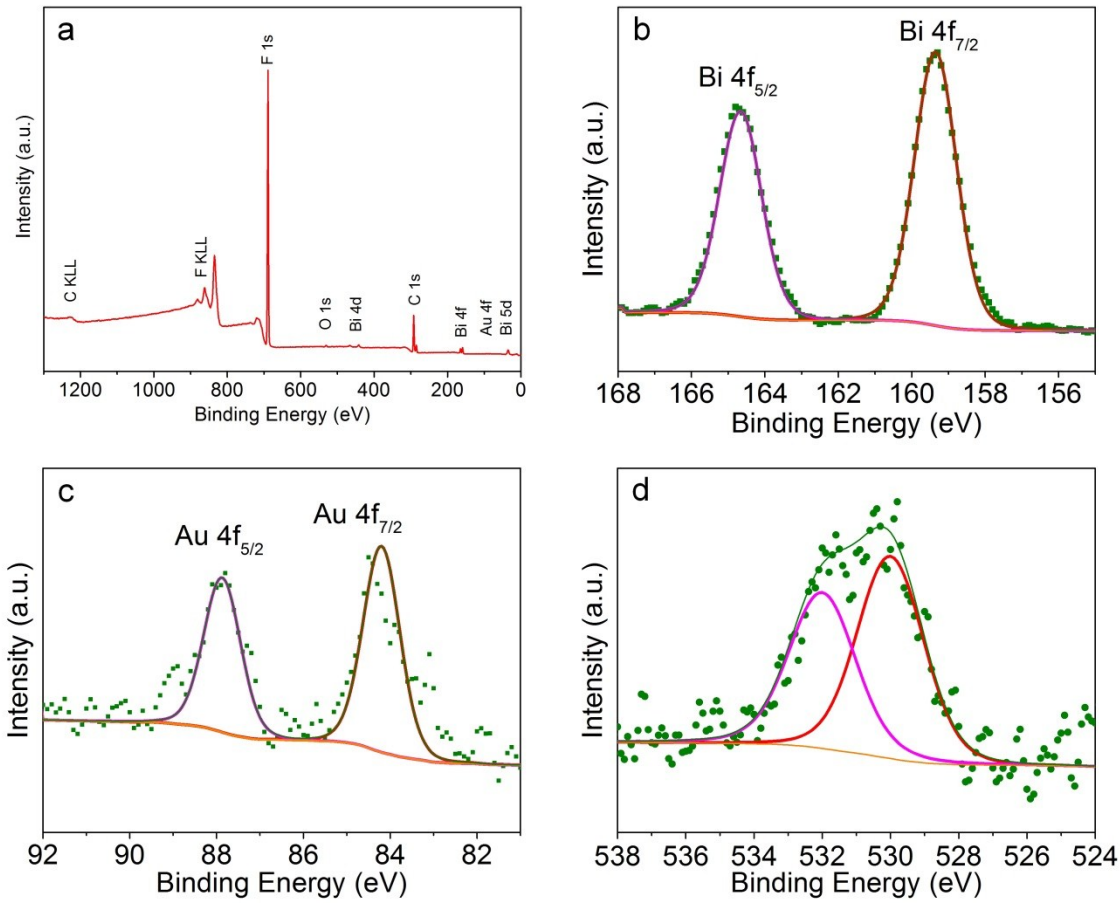

Figure S3. XPS spectra of Au-Bi_2O_3 with 5% Au before CO_2RR test: (a) survey spectrum, (b-d) high resolution spectra of (b) Bi 4f with the Bi $4f_{7/2}$ and Bi $4f_{5/2}$ peaks at 159.35 and 164.66 eV respectively, (c) Au 4f with the Au $4f_{7/2}$ and Au $4f_{5/2}$ peaks at 84.20 and 87.87 eV respectively, and (d) O 1s with a component peaked at 530.01 eV is assigned to the oxygen in metal oxides.

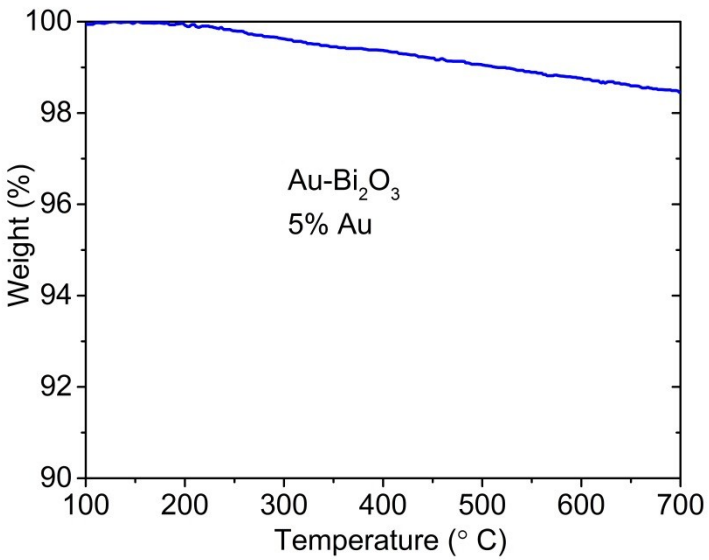

Figure S4. Thermogravimetric analysis (TGA) measurement of Au-Bi_2O_3 with 5% Au shows that the total carbon content on the surface of the fractal platform is less than 2%.

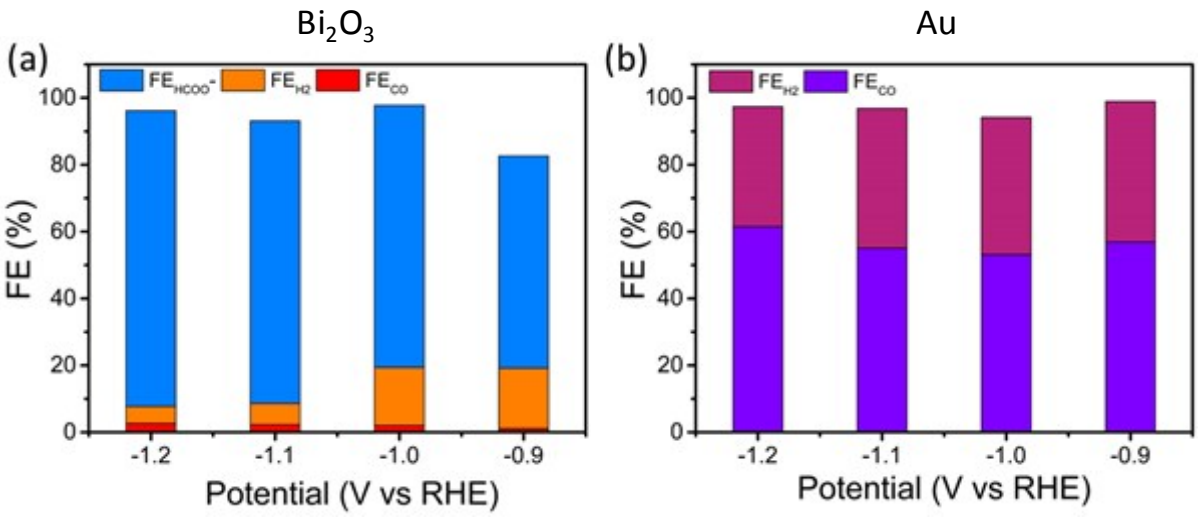

Figure S5. Dependence of Faradaic efficiency on applied potential for control **(a)** Bi_2O_3 and **(b)** Au on CFP in CO_2 saturated 0.1 M $KHCO_3$.

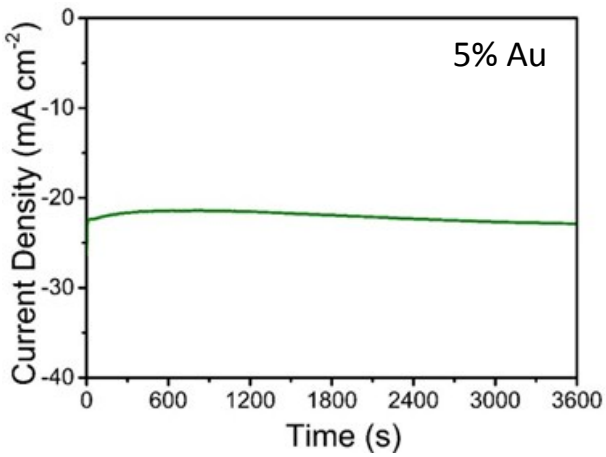

Figure S6. Representative chronoamperometry (*i-t)* curve for Au-Bi_2O_3 (5% Au) at -1.1 V vs RHE in CO_2 saturated 0.1 M $KHCO_3$.

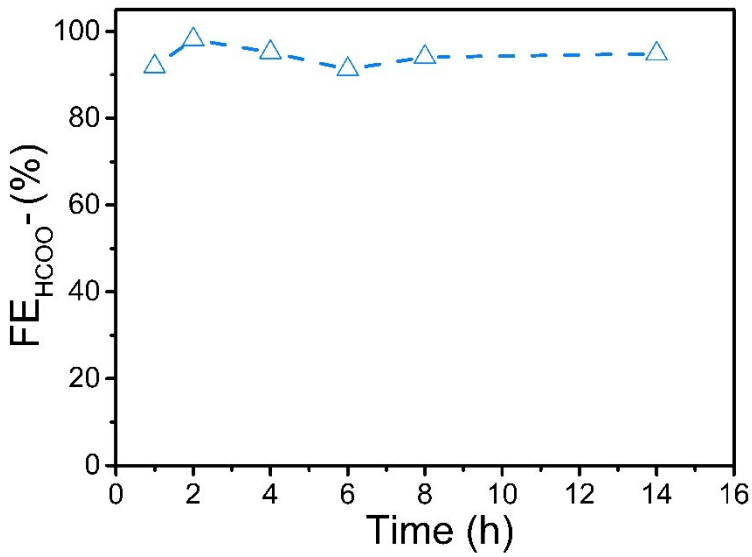

Figure S7. Stability testing results for Au-Bi_2O_3 at -1 V vs RHE in CO_2 saturated 0.1 M $KHCO_3$.

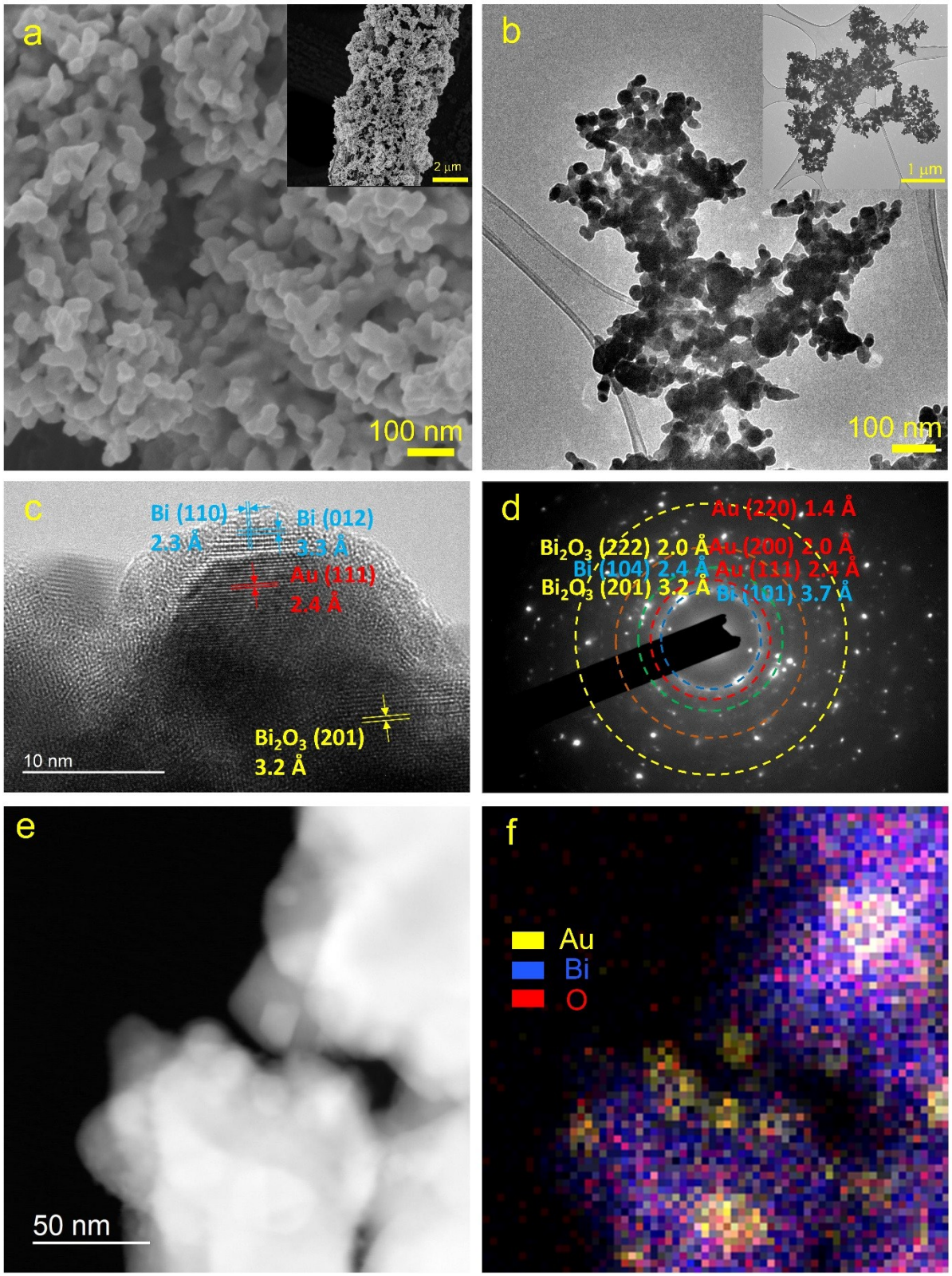

Figure S8. Morphological and compositional characterization of the Au-Bi_2O_3 (5% of Au) after CO_2RR. (a) SEM images, (b-c) TEM images of samples at different magnifications, (d) electron diffraction pattern, (e) HAADF STEM image and (f) EDS elemental mapping.

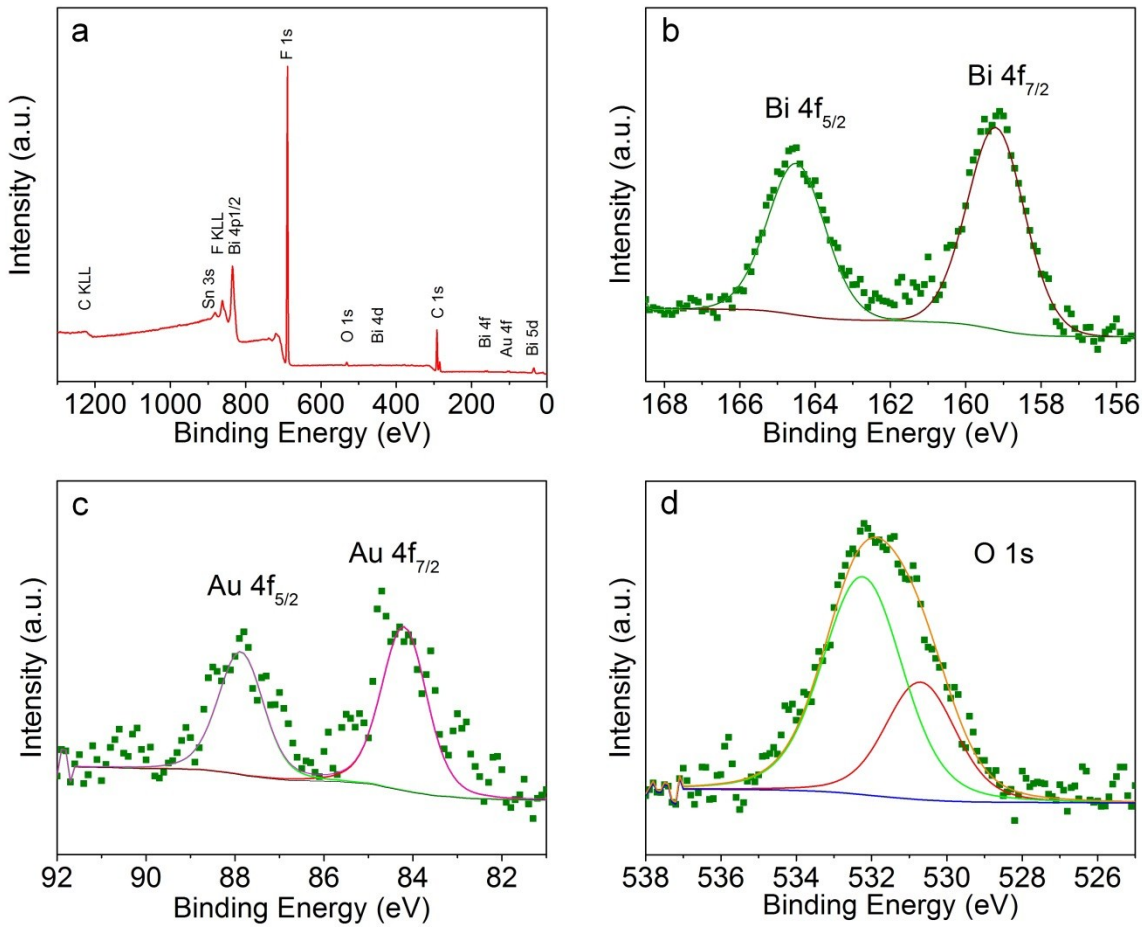

Figure S9. XPS spectra of Au-Bi_2O_3 with 5% Au after CO_2RR: (a) survey spectrum, (b-d) high resolution spectra of (b) Bi 4f with the Bi $4f_{7/2}$ and Bi $4f_{5/2}$ peaks at 159.20 and 164.50 eV respectively, (c) Au 4f with the Au $4f_{7/2}$ and Au $4f_{5/2}$ peaks at 84.20 and 87.87 eV respectively, and (d) O 1s with a component peaked at 530.73 eV is assigned to the oxygen in metal oxides.

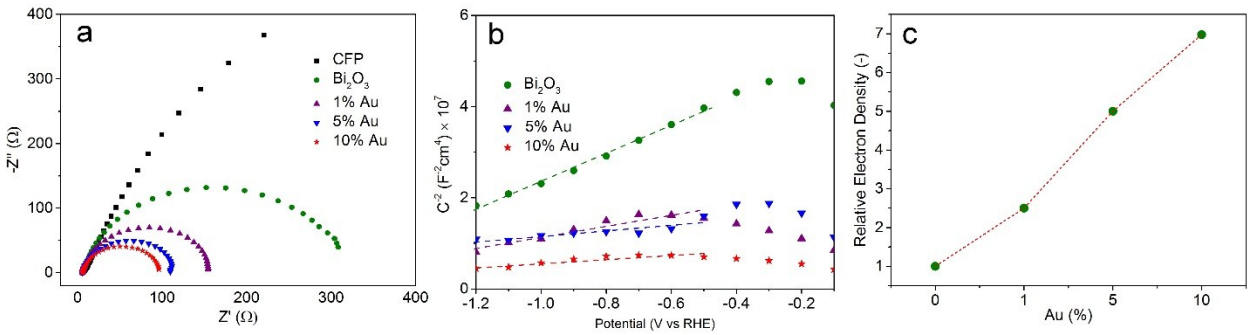

Figure S10. (a) Electron impedance spectroscopy (EIS), (b) Mott-Schottky (MS) analysis (the slope of the Mott-Schottky plot for each sample was linearly fitted in the potential window between -1.2 and -0.5 V), and (c) relative electron density of different Au concentration.

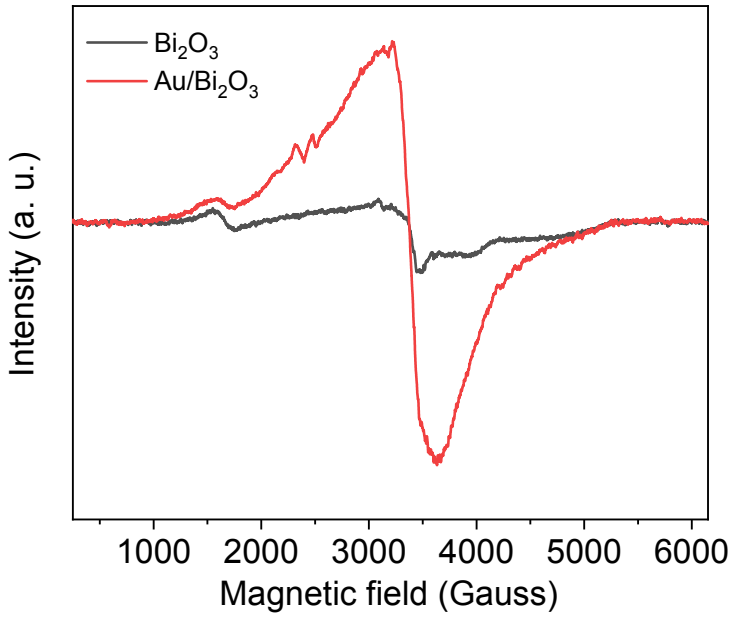

Figure S11. EPR spectra of Bi_2O_3 and Au-Bi_2O_3 (baseline subtracted). The spectra were obtained using 10.8 mg Bi_2O_3 and 9.0 mg Au/Bi_2O_3 under 120 K.

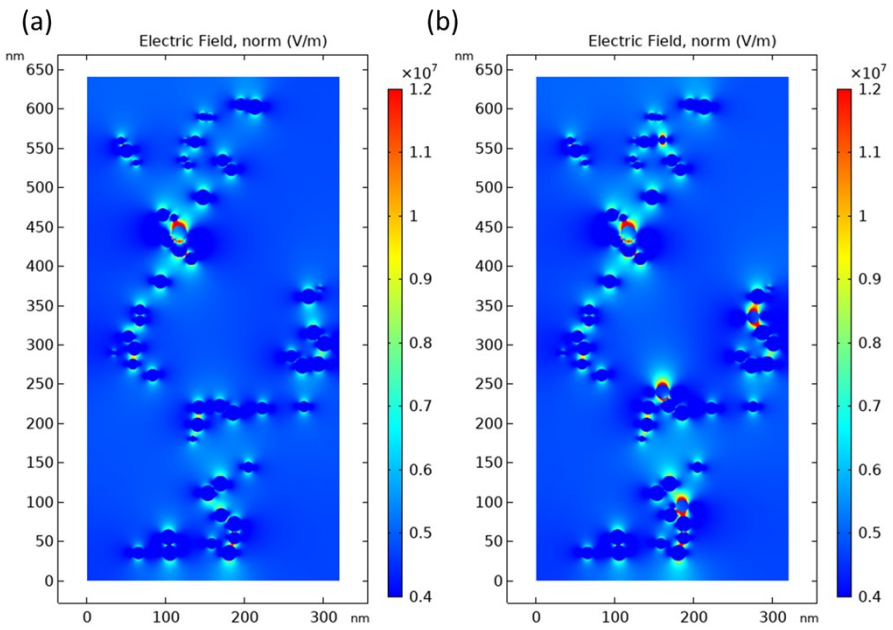

Figure S12. FEM simulation results demonstrating the distribution of the electric field in Bi_2O_3 containing **(a)** 1% and **(b)** 10% Au. More "hot edges" can be seen when the Au concentration was increased from 1% to 10%.

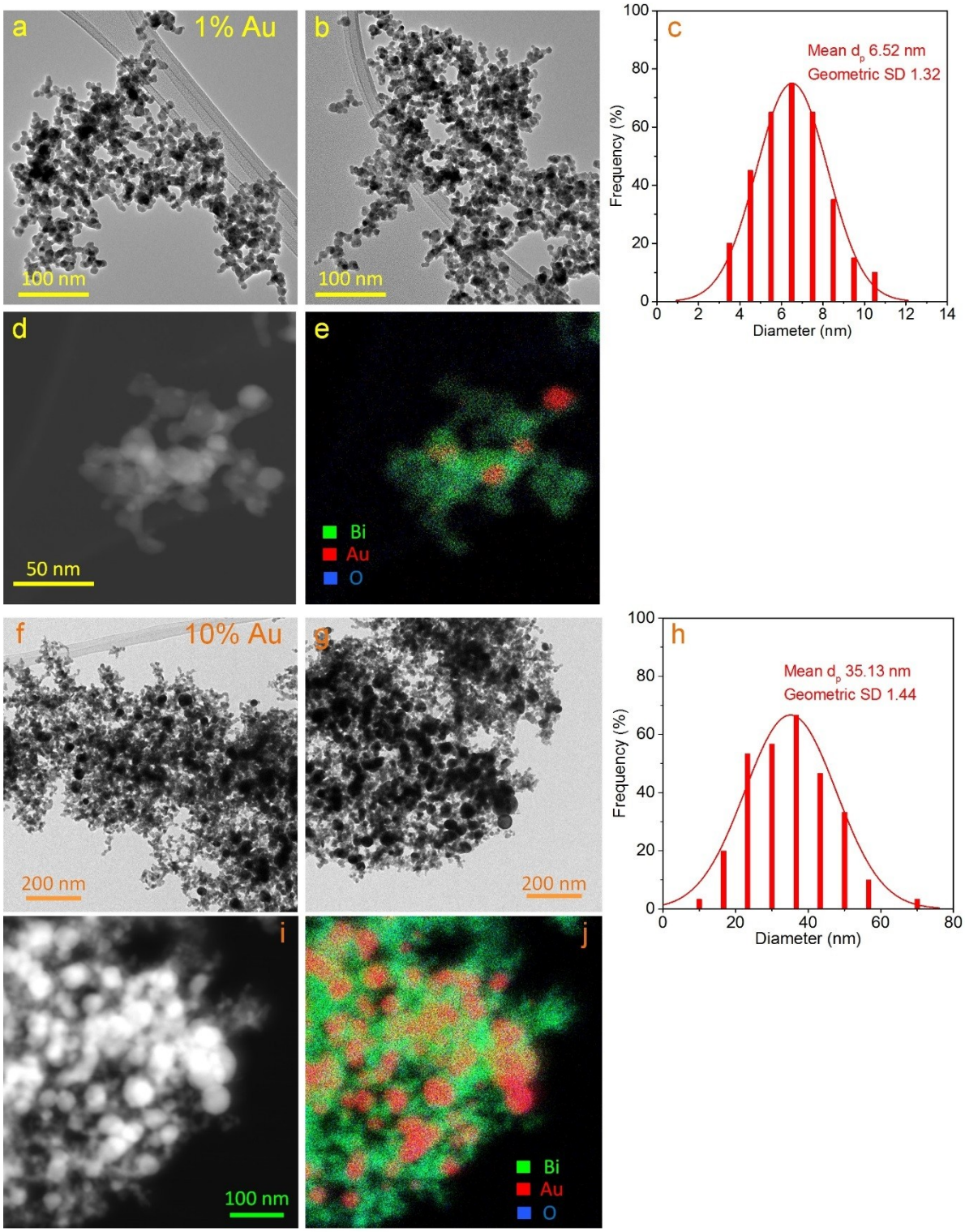

Figure S13. TEM images and histograms of the Au-Bi_2O_3 with different Au concentration. (a-c) 1% Au and (d-f) 10% Au. The mean of particle size has increased from 6.52 to 35.13 nm when the Au concentration increased from 1 to 10%. This increase leads to more Au surface exposed to the electrolyte to get involved into CO_2RR into CO product, resulting in an increase in the ratio of CO to formate product.

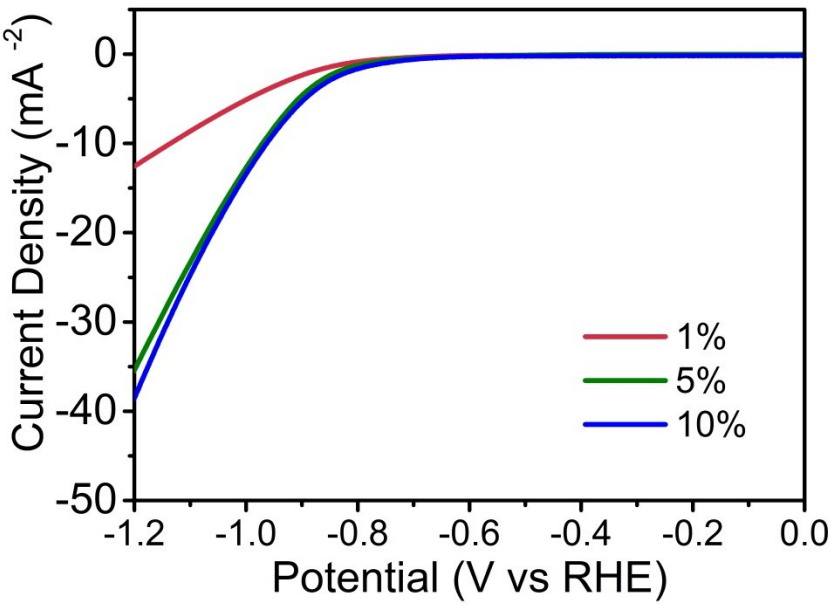

Figure S14. Dependence of current density on applied potentials for Au-Bi_2O_3 with different Au loading in CO_2 saturated 0.1 M $KHCO_3$.

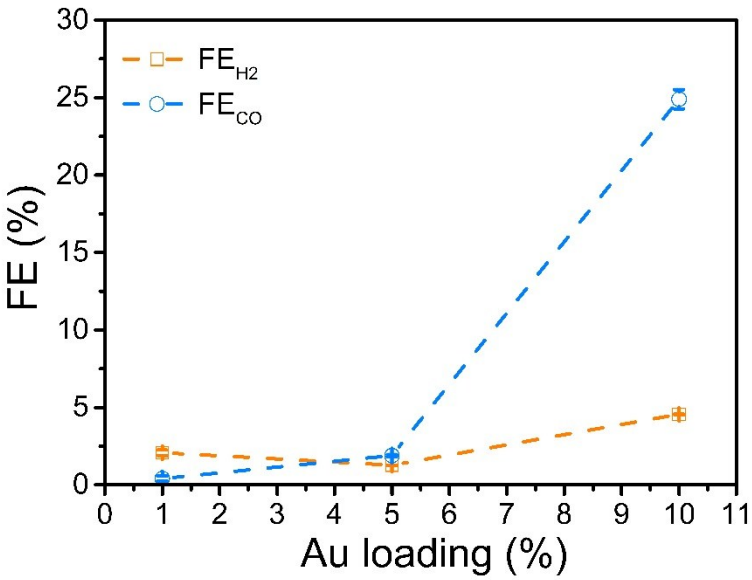

Figure S15. Dependence of FE_{H2} and FE_{CO} at -1.1 V vs RHE for Au-Bi_2O_3 with different Au loading in CO_2 saturated 0.1 M $KHCO_3$.

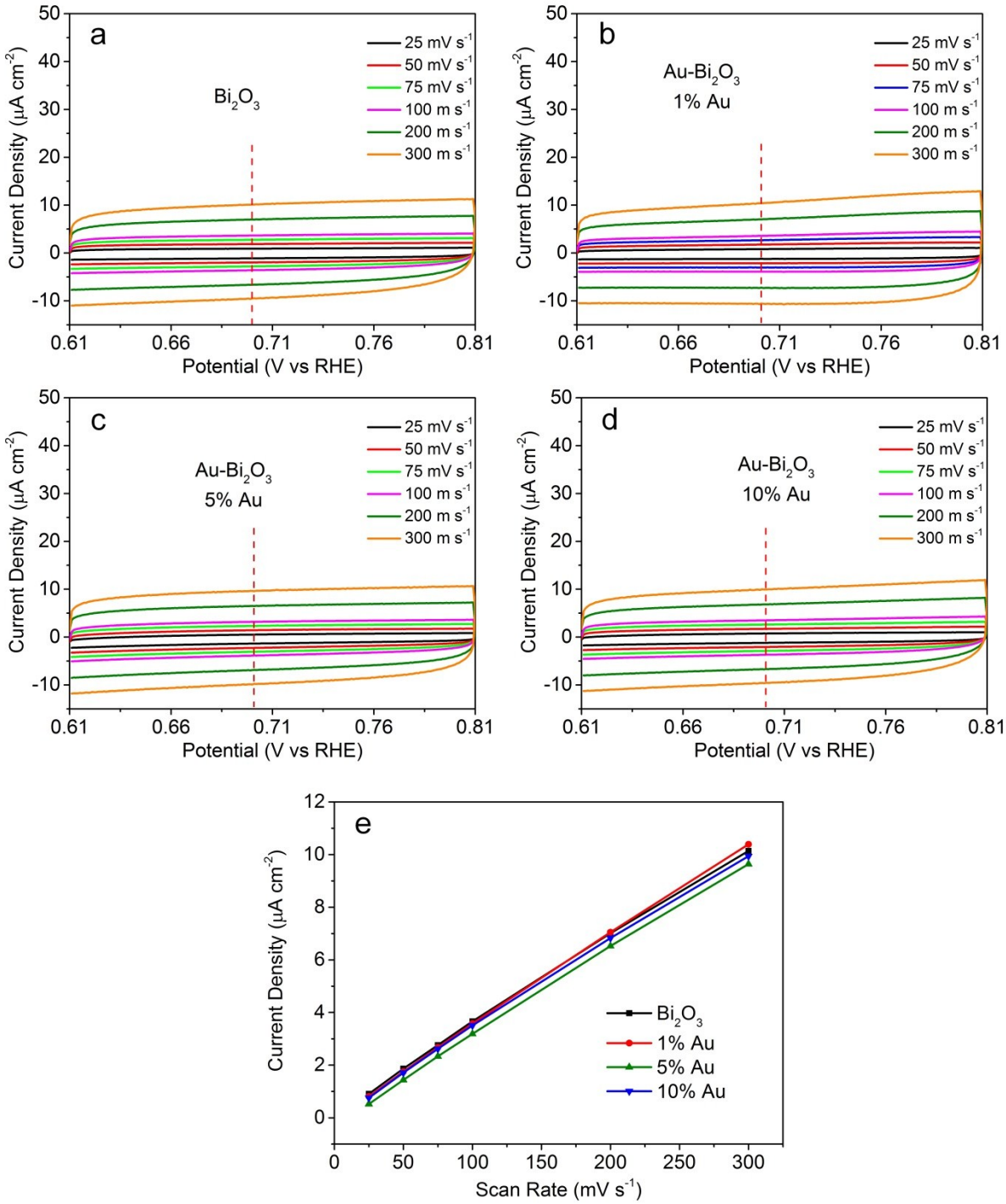

Figure S16. Cyclic voltammetry from different samples at different scant rates (a) Bi_2O_3, (b-d) Au-Bi_2O_3 with 1%, 5%, and 10% Au respectively, and (e) capacitive current vs scan rates plot at applied potential of 0.7 vs RHE for all samples.

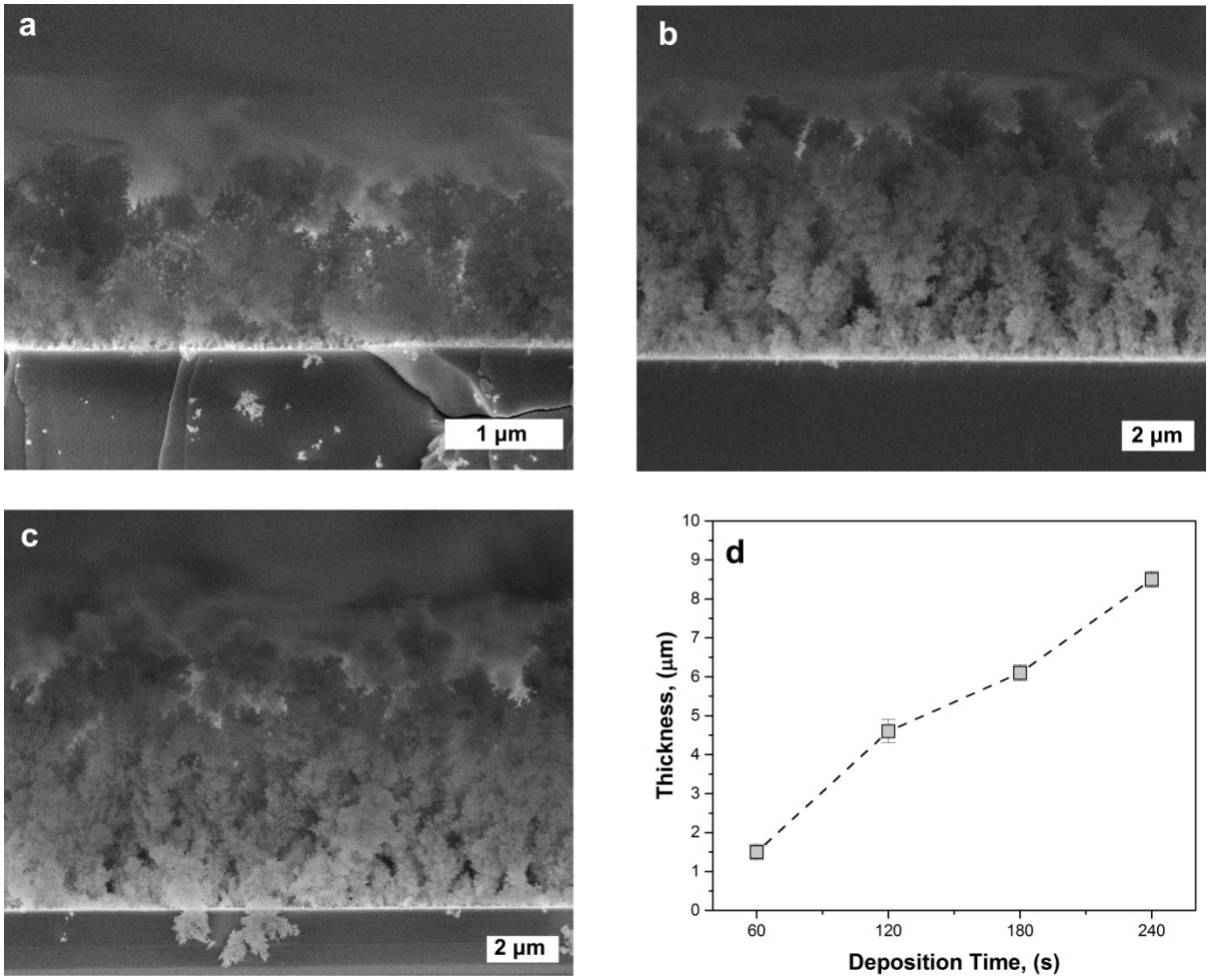

Figure S17. Growth rate. (a-c) Cross-sectional scanning electron microscope images of the 3D fractal Au (5%)-Bi_2O_3 metamaterials for aerosol deposition times of 1, 2 and 3 minutes, respectively. (d) Film thickness as a function of the deposition time indicates a linear growth rate, proving an excellent way for tuning the metamaterial properties.

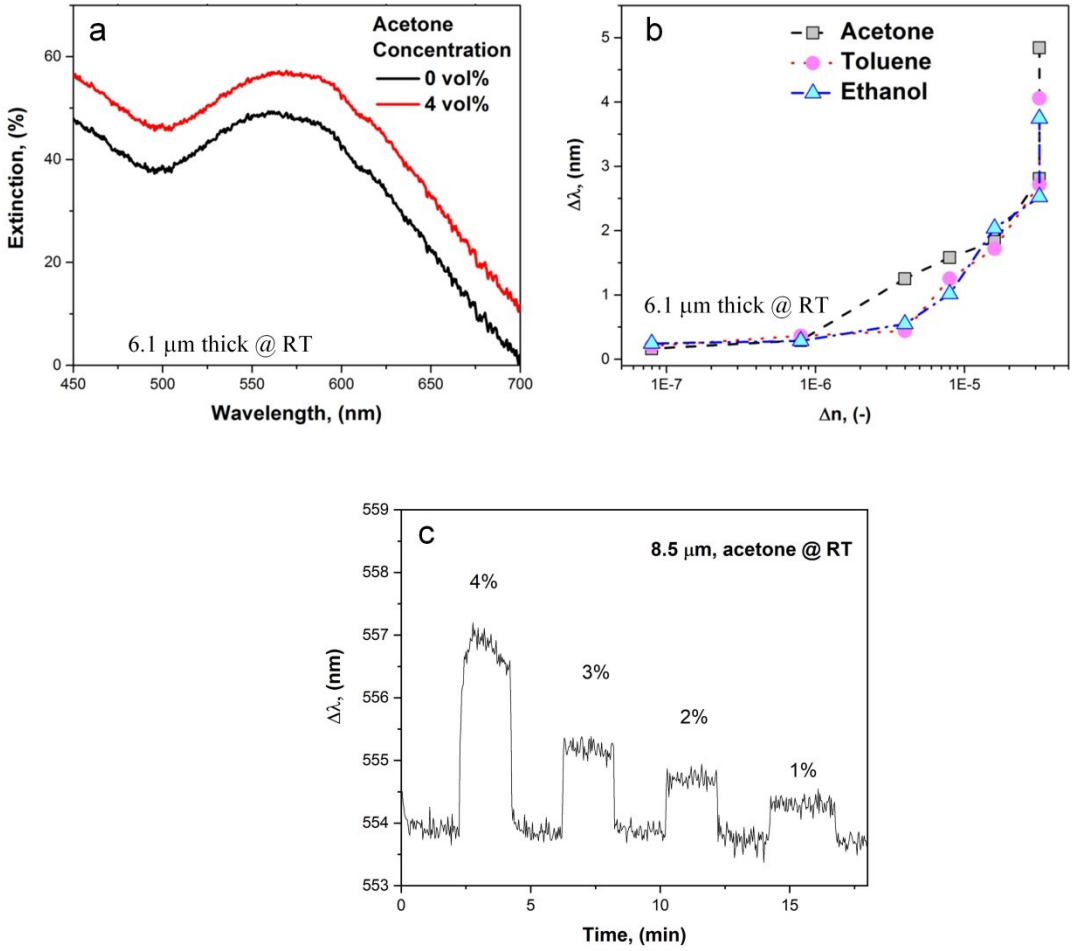

Figure S18. (a) Static extinction measurements of the 6.1 μm thick (3 min of deposition time) Au-Bi_2O_3 upon 4 vol% acetone injection at room temperature (RT). Note the drastic change that this VOC causes on the optical properties. (b) Plasmonic shift as a function of surrounding refractive index difference ($\Delta n = n_{gas} - n_{air}$) for the different tested VOCs. (c) Plasmonic wavelength shift upon different on/off injection cycles of acetone with different concentrations at room temperature for 8.5μm sample.

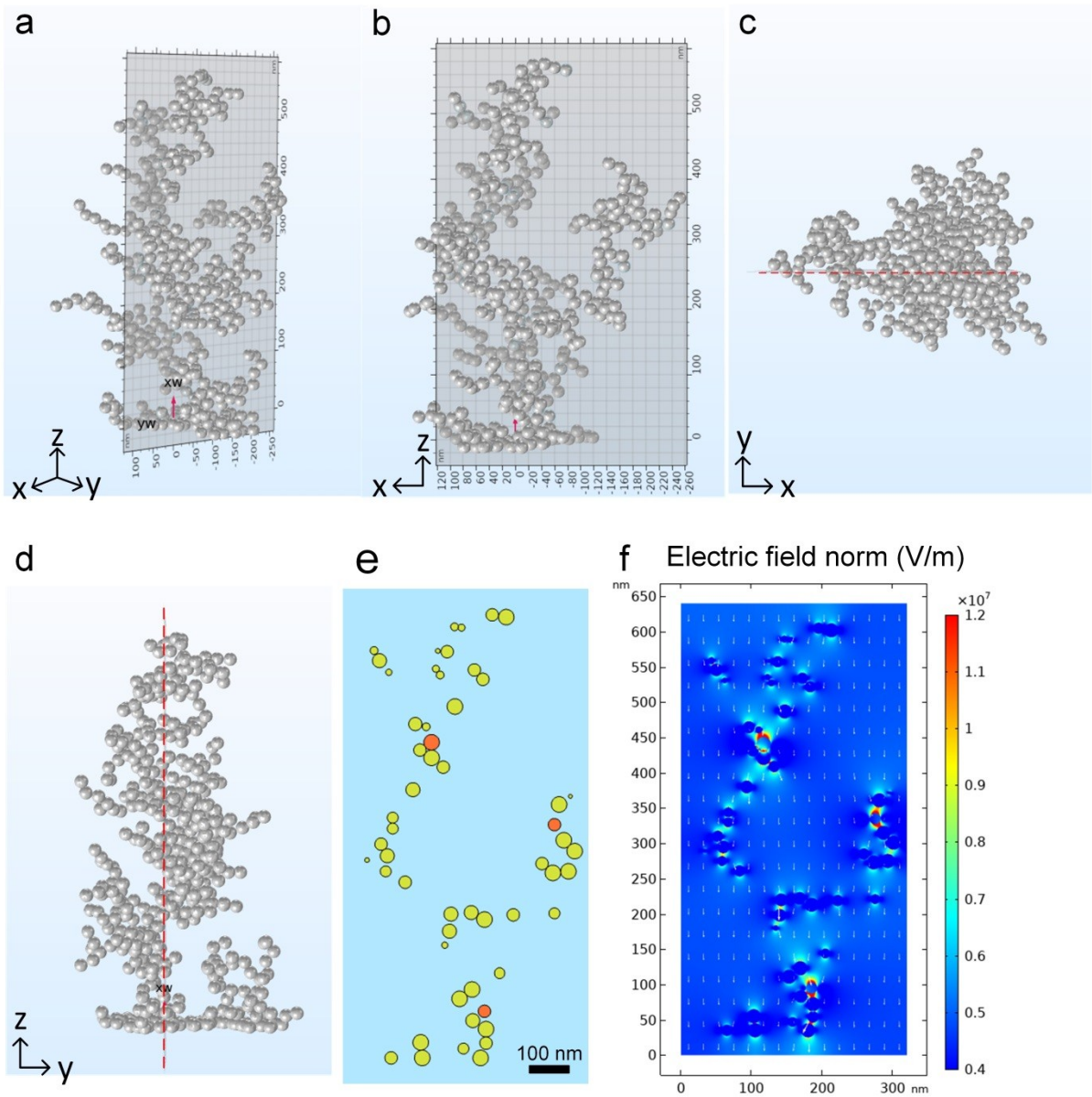

Figure S19. (a-d) The generated fractal structure of the 500 nm particles from different viewpoints with a plane cutting cross the structure to obtain the projection area, (e) the projection area obtained from the 3D structure of Bi_2O_3 (yellow) after adding three gold nanoparticles (red), and (f) electric field norm with flux distribution (arrow) obtained from the Electrostatics model from COMSOL Multiphysics.

Supporting Tables:

Table S1. CO_2RR catalytic performances of various Bi-based catalysts in similar operating conditions for $HCOO^-$ production.

Catalyst	Electrolyte	Onset Potential (V vs RHE)	Operating Potential (V vs RHE)	Current Density (mA/cm^2)	Mass specific formate partial current density (mA/mg)	Faradaic Efficiency for $HCOO^-$ (%)	Reference
Au-Bi_2O_3 fractal	**0.1 M $KHCO_3$**	**-0.6**	**-1.1**	**-22.6**	**-54**	**97**	**This Work**
Bi_2O_3 nanotubes derived Bi	0.5 M $KHCO_3$	-0.6	-1.0	-64	-60	~94	6
Bi-Sn	0.5 M $KHCO_3$ with 600 rpm stirring	-0.64	-1.14	-61	(Mass loading not provided)	94	7
Bi_2S_3 derived Bi	0.5 M $NaHCO_3$	-0.55	-0.75	-5	-14.7	84	8
Bi nanosheets	0.5 M $NaHCO_3$	-0.65	-0.9	-15	-15	99	9
Fractal-Bi_2O_3	0.1 M $KHCO_3$	-0.6	-1.2	-24	-52.2	87	10
Bi nanoparticles/Bi_2O_3 nanosheets	0.5 M $NaHCO_3$	-0.75	-0.85	-6	(Mass loading not provided)	~100	11
BiNS	0.5 M $NaHCO_3$	-1.3 V vs SCE	-1.5 V vs SCE	-14	-3.5	95	12
Eutectic Bi-Sn	0.1 M $KHCO_3$	-0.9	-1.1	-13	-10.1	78	13
Bi nanosheets	0.1 M $KHCO_3$	-0.5	-1.1	-16.5	-8.25	86	14

References

1. Karperien, A., FracLac for ImageJ, version 2.5. *Introduction. htm* **1999,** *2007*.
2. Fusco, Z.; Rahmani, M.; Bo, R.; Verre, R.; Motta, N.; Käll, M.; Neshev, D.; Tricoli, A., Nanostructured Dielectric Fractals on Resonant Plasmonic Metasurfaces for Selective and Sensitive Optical Sensing of Volatile Compounds. *Adv. Mater.* **2018,** *30* (30), 1800931.
3. Fazio, B.; Artoni, P.; Antonia Iatì, M.; D'Andrea, C.; Lo Faro, M. J.; Del Sorbo, S.; Pirotta, S.; Giuseppe Gucciardi, P.; Musumeci, P.; Salvatore Vasi, C.; Saija, R.; Galli, M.; Priolo, F.; Irrera, A., Strongly enhanced light trapping in a two-dimensional silicon nanowire random fractal array. *Light: Science &Amp; Applications* **2016,** *5*, e16062.
4. Sorensen, C. M., Light Scattering by Fractal Aggregates: A Review. *Aerosol Sci. Technol.* **2001,** *35* (2), 648-687.
5. Mandelbrot, B. B., *The fractal geometry of nature*. WH freeman New York: 1983; Vol. 173.
6. Gong, Q.; Ding, P.; Xu, M.; Zhu, X.; Wang, M.; Deng, J.; Ma, Q.; Han, N.; Zhu, Y.; Lu, J.; Feng, Z.; Li, Y.; Zhou, W.; Li, Y., Structural defects on converted bismuth oxide nanotubes enable highly active electrocatalysis of carbon dioxide reduction. *Nature Communications* **2019,** *10* (1), 2807.
7. Wen, G.; Lee, D. U.; Ren, B.; Hassan, F. M.; Jiang, G.; Cano, Z. P.; Gostick, J.; Croiset, E.; Bai, Z.; Yang, L., Orbital Interactions in Bi-Sn Bimetallic Electrocatalysts for Highly Selective Electrochemical CO2 Reduction toward Formate Production. *Adv. Energy Mater.* **2018,** *8* (31), 1802427.
8. Zhang, Y.; Li, F.; Zhang, X.; Williams, T.; Easton, C. D.; Bond, A. M.; Zhang, J., Electrochemical reduction of CO 2 on defect-rich Bi derived from Bi 2 S 3 with enhanced formate selectivity. *J. Mater. Chem. A* **2018,** *6* (11), 4714-4720.
9. Yang, H.; Han, N.; Deng, J.; Wu, J.; Wang, Y.; Hu, Y.; Ding, P.; Li, Y.; Li, Y.; Lu, J., Selective CO2 Reduction on 2D Mesoporous Bi Nanosheets. *Adv. Energy Mater.* **2018,** *8* (35), 1801536.
10. Tran-Phu, T.; Daiyan, R.; Fusco, Z.; Ma, Z.; Amal, R.; Tricoli, A., Nanostructured β-Bi2O3 Fractals on Carbon Fibers for Highly Selective CO2 Electroreduction to Formate. *Adv. Funct. Mater. 0* (0), 1906478.
11. Li, L.; Ma, D.-K.; Qi, F.; Chen, W.; Huang, S., Bi nanoparticles/Bi2O3 nanosheets with abundant grain boundaries for efficient electrocatalytic CO2 reduction. *Electrochim. Acta* **2019,** *298*, 580-586.
12. Han, N.; Wang, Y.; Yang, H.; Deng, J.; Wu, J.; Li, Y.; Li, Y., Ultrathin bismuth nanosheets from in situ topotactic transformation for selective electrocatalytic CO 2 reduction to formate. *Nature communications* **2018,** *9* (1), 1320.
13. Tang, J.; Daiyan, R.; Ghasemian, M. B.; Idrus-Saidi, S. A.; Zavabeti, A.; Daeneke, T.; Yang, J.; Koshy, P.; Cheong, S.; Tilley, R. D.; Kaner, R. B.; Amal, R.; Kalantar-Zadeh, K., Advantages of eutectic alloys for creating catalysts in the realm of nanotechnology-enabled metallurgy. *Nature Communications* **2019,** *10* (1), 4645.
14. Zhang, W.; Hu, Y.; Ma, L.; Zhu, G.; Zhao, P.; Xue, X.; Chen, R.; Yang, S.; Ma, J.; Liu, J., Liquid-phase exfoliated ultrathin Bi nanosheets: Uncovering the origins of enhanced electrocatalytic CO2 reduction on two-dimensional metal nanostructure. *Nano energy* **2018,** *53*, 808-816.